ENVIRONMENTAL RESEARCH
LETTERS

OPEN ACCESS

RECEIVED
8 June 2024

REVISED
21 November 2024

ACCEPTED FOR PUBLICATION
23 December 2024

PUBLISHED
5 February 2025

Original content from this work may be used under the terms of the Creative Commons Attribution 4.0 licence.

Any further distribution of this work must maintain attribution to the author(s) and the title of the work, journal citation and DOI.

LETTER

Under a not so white sky: visual impacts of stratospheric aerosol injection

Ansar Lemon[1,*], **David W Keith**[2] and **Steve Albers**[3]

[1] School of Engineering and Applied Sciences, Harvard University, Cambridge, MA 02138, United States of America
[2] Climate Systems Engineering Initiative, Department of Geophysical Sciences, University of Chicago, Chicago, IL 60637, United States of America
[3] (Ret.) Cooperative Institute for Research in the Atmosphere, Colorado State University, Fort Collins, CO 80521, United States of America
[*] Author to whom any correspondence should be addressed.

E-mail: ansar_lemon@g.harvard.edu

Keywords: stratospheric aerosol injection, solar geoengineering, sky appearance, sky visuals, climate change, perceptual science, chromaticity analysis

Supplementary material for this article is available online

Abstract

Stratospheric aerosol injection (SAI) could change the sky's appearance. This could play a role in shaping public perception of SAI. Noticeability depends strongly on tropospheric aerosol optical depth (AOD) and the amount of SAI used. We aim to quantify the noticeability of changes in sky color and brightness due to SAI. We use a 3D visible light radiative transfer package to generate cloudless sky images during high sun, sunset, and twilight under SAI from the reference point of a ground observer. We consider three aerosol types: H_2SO_4, $CaCO_3$, and diamond. We consider stratospheric aerosol loadings required to produce radiative forcings of -1, -2, and -4 W m^{-2}. We use population density and AOD data to compute the distribution of AODs people experience and then simulate sky images for the 10th, 50th, and 90th percentiles of that distribution. We compare the simulated changes in color and brightness to experimental measurements of minimum thresholds humans can detect. The three aerosol types cause similar changes, except most notably the diamond aerosol increases brightness of the solar aureole by roughly three to five times less than do H_2SO_4 or $CaCO_3$. During high sun, sky whitening from sulfate SAI at -2 W m^{-2} is undetectable for roughly half of observers chosen randomly from the global population. For the remainder of the population, we expect whitening to still be unnoticeable for all but perhaps the most astute observers aided by color samples. Brightening and enlargement of the solar aureole is the most visible feature during high sun for H_2SO_4 and $CaCO_3$, while changes near twilight would be the most noticeable impact of SAI. We cannot evaluate the fraction of the population who would notice these changes.

1. Introduction

Solar radiation management through stratospheric aerosol injection (SAI) may reduce some aspects of climate change such as rising global average temperatures [1], increasing regional temperature and precipitation extremes [2], and ice sheet melting [3]. However, it could also cause side effects such as changes in ozone layer thickness and stratospheric heating [4], differences in UV radiation exposure [5], and regionally disparate climate impacts [6]. Many of the risks associated with solar geoengineering have been extensively studied over the last decade, yet the possible effects of SAI on the sky's appearance have received little analytical attention despite the possibility that they play a significant role in shaping public perception of SAI.

In his '20 Reasons Why Geoengineering May Be a Bad Idea' [7], Alan Robock listed whitening of the sky under SAI. A prominent environmental author highlighted the concern in her book title 'Under a White Sky' [8]. However, we are aware of only one paper [9] which studied the visual impacts of SAI. In that study, Kravitz *et al* computed spectral irradiance at

© 2025 The Author(s). Published by IOP Publishing Ltd

the point of a ground observer under sulfate-based SAI during daytime and sunset, using enough aerosol to offset warming from up to a doubling of atmospheric CO_2 relative to that of the preindustrial era. They concluded that the added sulfate layer would cause sky visuals very similar to those following volcanic eruptions with a whitening of the sky during the day and afterglows during sunset, as well as a general increase in sky brightness or diffuse irradiance.

While Kravitz *et al* calculated total spectral irradiance [9], we instead calculate spectral radiance at three wavelengths chosen to represent human vision for zenithal and azimuthal angles relative to a ground observer and generate full images of the sky. We simulate sky images for three different SAI aerosol types, with loading amounts corresponding to three different levels of radiative forcing. We then compare changes in sky chromaticity and brightness to minimum human detection thresholds measured in perceptual studies. Since these thresholds were derived through controlled experiments with participants seeking differences in side-by-side comparisons [10, 11], we expect these noticeability metrics to be significantly more sensitive than human perception in the real world. We therefore estimate upper bounds on real-world noticeability of changes in the sky's appearance due to SAI. We perform simulations for a clear sky with no clouds, highlighting any possible changes in color or brightness during high sun.

The amount of tropospheric aerosol strongly determines the noticeability of SAI, so we estimate the frequency distribution of tropospheric aerosol optical depth (AOD) seen by a random human. We use this distribution to investigate the fraction of the population that might notice SAI under various assumptions.

2. Methods

We use the 3D visible light radiative transfer package Simulated Weather Imagery (SWIm) [12] to generate clear sky images from the reference point of a ground observer under SAI during daylight, sunset, and twilight. We consider three different injection aerosol types: sulfate, calcite, and diamond. For each, we consider loading amounts corresponding to three different radiative forcing levels: -1, -2, and -4 W m^{-2}. We consider background tropospheric aerosol loading amounts corresponding to the average experienced by 10%, 50%, and 90% of the human population. We use color analysis through chromaticity spaces as defined by the International Commission on Illumination (CIE), previously used in other studies regarding sky appearance, to quantify the visibility of changes in sky color [13, 14]. We use spectral diffuse radiance data to quantify the visibility of changes in sky brightness.

We first define the optical properties and size distributions of the SAI aerosols. We then calculate the stratospheric AOD required for each aerosol species to generate each level of radiative forcing. We compute the global frequency distribution of population-weighted total atmospheric AOD using satellite observation and population distribution data. We use the population-weighted AOD distribution to choose representative samples for tropospheric AOD. Finally, using the SAI AOD values and the representative tropospheric AOD values, we use SWIm to generate simulated images with chromaticity and spectral radiance data for the sky's appearance under various scenarios.

2.1. SAI aerosol properties

We consider three SAI aerosol types: H_2SO_4, $CaCO_3$, and diamond. While H_2SO_4 is the most studied SAI aerosol, $CaCO_3$ and diamond have been proposed as alternatives for less stratospheric heating and ozone loss [15, 16]. For each aerosol, we assumed refractive index properties matching those given by Dykema *et al* [17].

Table 1 shows the assumed aerosol size distributions. The size distribution of sulfate aerosol depends on the injection method. Our size distribution for H_2SO_4 was chosen to roughly correspond to use of methods such as injection of accumulation-mode aerosol that steers the overall aerosol size distribution towards the optimal size (see figure A1) [18]. The size distributions for $CaCO_3$ and diamond were assumed to be normal with 95% of each distribution within $\pm$25% of the corresponding mean value to represent manufactured solid particles. Subject to these constraints, size distribution parameters were calculated for each aerosol such that the resulting effective radius was optimal for achieving maximum radiative forcing versus fixed mass [17].

Kravitz *et al* thoroughly investigated the effect of changes in size distribution parameters on the forward scattering properties of sulfate aerosol [9]. We expect moderate changes in σ to not significantly affect our results. However, larger median radii could increase whitening for sulfate (see figure A4). We see an example of this with our volcanic sulfate simulations.

2.2. Pinatubo aerosol properties

The Pinatubo aerosol is composed of H_2SO_4 with the size distribution shown in table 1 and an optical depth of 0.120 at wavelength 550 nm. These match those used by Kravitz *et al* [9] and represent approximate values measured 9 months after the eruption of Mount Pinatubo in 1991 [19, 20]. We assumed the same refractive index properties as for our SAI sulfate aerosol.

2.3. Radiative forcing

We used the shortwave component of the Rapid Radiative Transfer Model (RRTMG_SW) [21, 22] to calculate globally, annually averaged radiative

Table 1. The chosen size distribution type with corresponding μ and σ parameters for each SAI aerosol type. The resulting effective radius of each size distribution is also shown.

Aerosol type	Size distribution type	μ	σ	Effective radius (μm)
H_2SO_4	Log-normal	−1.420	0.300	0.300
$CaCO_3$	Normal	0.267	0.033	0.275
Diamond	Normal	0.146	0.018	0.150
Pinatubo	Log-normal	−0.910	0.336	0.524

shortwave flux for each of the three SAI aerosols. These calculations were used to derive the SAI stratospheric AODs required to produce shortwave radiative forcings −4, −2 and −1 W m^{-2}. Longwave forcing would reduce the net radiative forcings of sulfate by about 20%, with smaller changes for $CaCO_3$ and diamond [16, 17]. Today, the total anthropogenic radiative forcing is approximately +2.72 W m^{-2} relative to that of the preindustrial era [23], so these are sizable interventions requiring multiple decades of ramp up in a realistic deployment scenario. The value −4 W m^{-2} was chosen to represent enough solar geoengineering to balance out the radiative forcing from roughly a doubling of atmospheric CO_2 relative to that of the preindustrial era [24]. The values −2 and −1 W m^{-2} were chosen to represent more moderate scenarios in which solar geoengineering is gradually increased so it offsets less than half of greenhouse gas climate forcing late this century [25], providing global cooling of roughly −1 and −0.5 °C respectively [24, 26].

The background atmosphere in RRTMG_SW was set to that of a 51-layer clear-sky midlatitude summer standard atmosphere. Cloud albedo was incorporated by adjusting the surface albedo profile to replicate zonal and monthly averages of the observed all-sky albedo. The observed all-sky albedo was the top of the atmosphere all-sky product from the year 2022 of CERES_EBAF_Ed4.2 [27, 28].

A globally uniform stratospheric aerosol layer was used to represent SAI. While realistic deployments would produce non-uniform AODs, global mean AODs should roughly match the values calculated here. Mie theory was used to compute the single-scattering albedo, asymmetry parameter, and sample AOD input parameters for each aerosol (see tables A1–A2). Radiative forcing was calculated as the difference in globally, annually averaged net shortwave flux at the top of the atmosphere with and without SAI. Using linear extrapolation, we computed the AOD values necessary to achieve the desired radiative forcings −4, −2 and −1 W m^{-2} (see figure A2). The resulting AODs are shown in table 2. The AOD values calculated for H_2SO_4 were found to approximately match those in prior literature [29, 30].

Table 2. The calculated aerosol optical depths at wavelength 550 nm needed for a globally uniform stratospheric aerosol layer composed of each SAI aerosol type to achieve each of three levels of globally, annually averaged radiative forcing.

Radiative forcing	AOD (H_2SO_4)	AOD ($CaCO_3$)	AOD (Diamond)
−1 W m^{-2}	0.042	0.041	0.025
−2 W m^{-2}	0.084	0.082	0.050
−4 W m^{-2}	0.169	0.165	0.100

2.4. Background tropospheric aerosol

We use daily total atmospheric AOD data from the year 2022 of the MERRA-2 dataset [31] to approximate present-day conditions (see figure B1), combined with global population density from the year 2020 of the UN WPP-Adjusted Population Density v4.11 dataset [32], to calculate cumulative probability distributions for AOD seen by a random observer. Stratospheric AOD was small in 2022, so we neglect it and use the data here to represent tropospheric AOD.

2.5. Image simulation

We used SWIm, a visible-wavelength three-dimensional radiative transfer model, to simulate ground-based observer images of a cloudless sky under different SAI scenarios for daytime, sunset, and twilight conditions. For a given location, time, and atmospheric composition, it generates visually and physically realistic hemispheric or 360° spherical panoramic color images of the atmosphere and the underlying terrain from a specified vantage point [12]. It takes a variety of inputs. For the stratosphere, we can set the background aerosol AOD and composition, as well as scattering properties for additional aerosols including single-scattering albedo, angstrom exponent, and modified Henyey–Greenstein phase function parameters which are used to approximate the Mie phase function. For the troposphere, we can set the background aerosol AOD and composition. Other inputs consist of solar zenith angle, viewpoint altitude, and hydrometeor fields. SWIm performs ray tracing calculations at three reference wavelengths corresponding to primary colors of human perception: 615 nm, 546 nm, and 450 nm.

For each SAI aerosol, we first used Mie theory to calculate the single-scattering albedo at each reference wavelength used by SWIm. We then calculated the angstrom exponent between 450 nm and 615 nm (see table A3). We next calculated Mie phase functions at each reference wavelength and used non-linear least squares curve fitting to determine best fit modified Henyey–Greenstein phase function parameters utilized by SWIm (see table A4 and figure A3).

We used these aerosol scattering properties, the previously calculated SAI stratospheric AODs corresponding to radiative forcing levels −4, −2, −1 and 0 W m^{-2}, and the 90th, 50th, and 10th percentile population-weighted tropospheric AOD values as inputs to SWIm. A background stratospheric AOD equal to 0.005 composed of sulfates was added, roughly representing global mean satellite measurements in years prior [33]. The tropospheric AOD composition was set to 50% organic carbon and 50% dust as these are representative species at many continental locations [34]. To represent daytime, sunset, and twilight conditions we used solar zenith angles of 29°, 88°, and 96° respectively. The viewpoint altitude was set to sea level. The viewpoint latitude and longitude were set (arbitrarily) to that of Boston, Massachusetts. The simulation day was set to 28 May 2023. Because we assumed cloud-free conditions, no hydrometeor field was used.

2.6. Image analysis

While Kravitz *et al* present sky colors as metameric matches and sky brightness changes as ratios of visible band irradiance, here we go a step further by calculating sky color and brightness changes in terms of minimum thresholds for human detection found in perceptual studies. These thresholds were measured through controlled experiments where observers compared color or brightness differences through side-by-side comparisons. Our estimates should therefore be interpreted as upper bounds on real-world noticeability, as they do not include the effects of time and memory on perception.

To quantify changes in sky color we used chromaticity analysis consistent with some prior sky color analysis [13, 14]. For the sky images simulated in the previous step, we used SWIm to generate corresponding principal plane chromaticity data in the CIE 1931 color space and diffuse spectral radiance values at each of the three reference wavelengths. We converted the chromaticity data from (x, y) values in the CIE 1931 color space to (u', v') values in the more spatially uniform CIE 1976 color space. To describe color differences in terms of distance in this color space, we defined a just noticeable difference in color (JND_C) as the radius (0.0033) of 3-step $u'v'$ circles [10]. This JND_C value is used as the approximate threshold for human detection of color change. There remains much uncertainty in how best to characterize a JND_C, and using the radius of smaller 1.18-step $u'v'$ circles is also suggested as a possible alternative [10]. For each tropospheric AOD value, the magnitude distance between chromaticity points for scenarios with and without SAI were computed and converted into JND_C values versus viewer zenith angle.

To quantify changes in sky brightness, we first multiplied each diffuse spectral radiance by the value of the Judd–Vos modified CIE 1931 eye sensitivity function at the corresponding reference wavelength [35]. This weighted the radiances according to human eye sensitivity. We then computed the sum of these radiances across the three wavelengths. For each tropospheric AOD value, the percentage difference between radiance sums for scenarios with and without SAI were computed versus viewer zenith angle. We defined a just noticeable difference in brightness (JND_B) as 7.4%. This value was experimentally determined to be the minimum threshold for human detection of illuminance difference in a controlled light box experiment [11].

3. Results

Figure 1 shows Mie phase functions for the three SAI aerosols. H_2SO_4 and $CaCO_3$ have nearly identical forward scattering, and hence backscattering, across all three visible wavelengths. Diamond has less forward scattering, and hence more efficient backscattering, across all three visible wavelengths. It also has stronger scattering at angles greater than roughly 60°. The backscattering efficiency comparisons are evident in the stratospheric AODs necessary for each aerosol type to achieve a given radiative forcing (table 2). The AODs required for H_2SO_4 and $CaCO_3$ to achieve the same radiative forcing are nearly equivalent, while Diamond requires approximately 30%–40% less.

Figure 2 shows cumulative probability distributions of tropospheric AOD. The population-weighted values are largest, highlighting the correlation between where people live and the presence of atmospheric aerosols, particularly pollution aerosols. For the results that follow, we use the 10th, 50th, and 90th percentile population-weighted values. On a random day, for instance, on average only 10% of the global population would experience AOD values that are at or below the 10th percentile value.

Figure 3 shows example simulated polar sky images with and without SAI (see more in figures C1–C3). While these polar images can represent effects in a concise form, additional simulation images can be viewed at https://simulatesrm.github.io/. In figure 3, we observe similar visual impacts from H_2SO_4 and $CaCO_3$ at equivalent levels of radiative forcing. From diamond, we see a significantly lower increase in brightness, particularly in the solar aureole during high sun. This agrees with the scattering properties observed in figure 2. Across all three aerosols we see whitening due to SAI during high sun and reddening during twilight.

The high sun whitening and twilight reddening effects can be confirmed by looking at the chromaticity diagrams in figure 4 (see more in figure D1). During high sun, chromaticity points corresponding to added SAI trend towards the white point. During twilight, chromaticity points corresponding to added SAI approximately trend towards the red portion of the CIELUV color space.

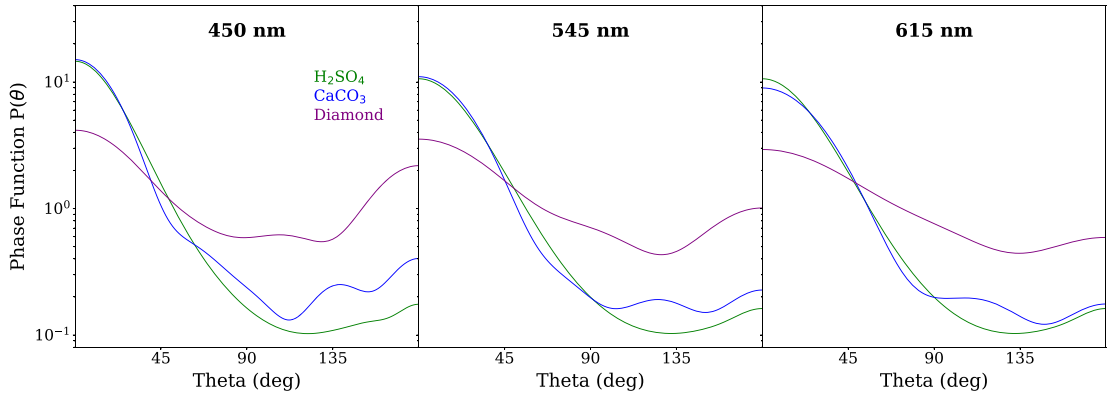

Figure 1. Mie phase functions at each of three reference wavelengths, averaged over corresponding size distributions for each of three SAI aerosol types. The phase functions were normalized such that integration over all solid angles equals 4π.

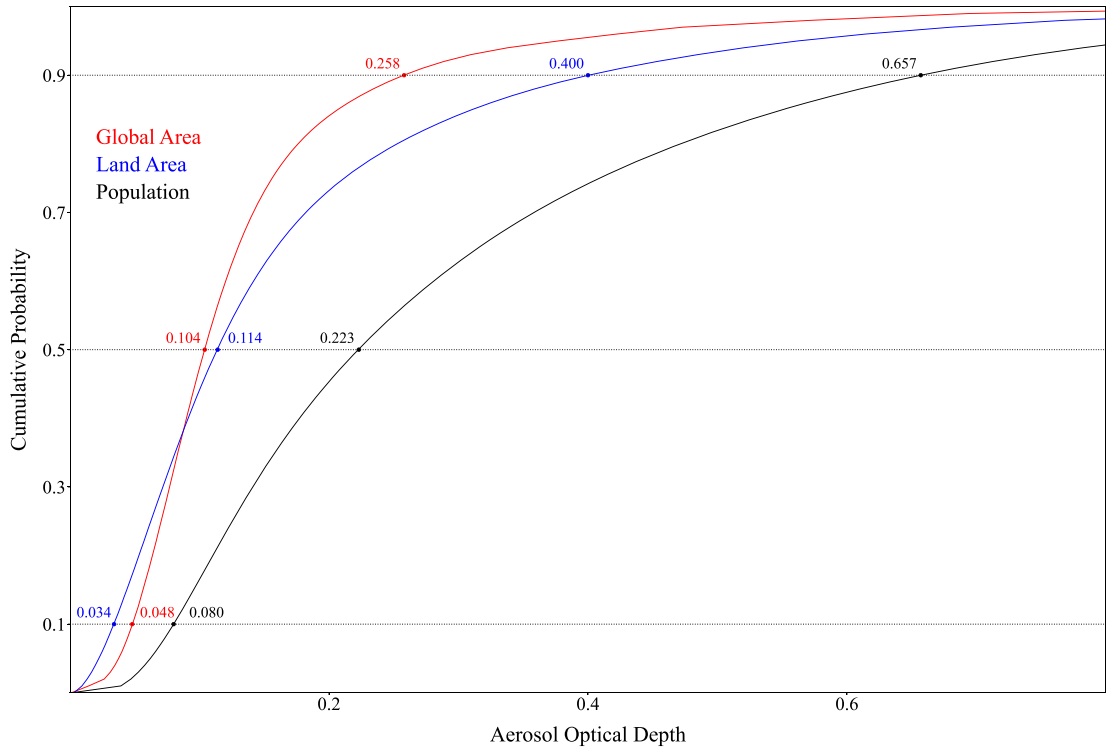

Figure 2. Cumulative probability distribution of daily total atmospheric aerosol optical depth (AOD) weighted by population (black), land area (blue), and global area (red). The AOD data is from the year 2022 of the MERRA-2 dataset. The 10th, 50th, and 90th percentile AODs are marked on the curves.

Figure 5 examines changes in sky color under -2 W m^{-2} of SAI (see more in figure D2). Plotted are absolute changes in chromaticity, not chromaticity changes towards a specific color. The changes due to H_2SO_4 and $CaCO_3$ exhibit roughly the same distribution and similar magnitudes, with roughly uniform changes in color on either side of the sun. For diamond, the color changes are much more focused approximately 90° away from the sun. This is consistent with diamond's scattering phase function which has strong scattering for all three reference wavelengths around 90°. The Pinatubo aerosol causes larger peak color changes than do any of the three SAI aerosols. Its larger particle size also focuses color changes closer to the sun.

Figure 6 examines changes in sky brightness under -2 W m^{-2} of SAI (see more in Figure D3). All three aerosols increase visible sky brightness. The increase from H_2SO_4 and $CaCO_3$ is greatest near the sun, while that from diamond is greatest approximately 90° away from the sun. This difference highlights the lower forward scattering of diamond. All increases taper off towards the horizon. Overall, we see lower peak brightness increases from diamond. The Pinatubo aerosol causes roughly double the peak brightness increase from H_2SO_4 or $CaCO_3$. This is

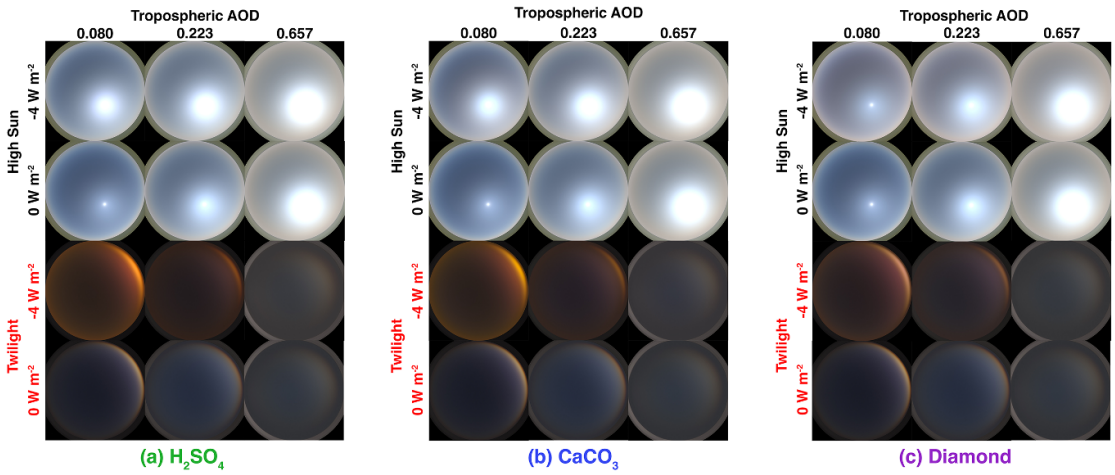

Figure 3. Simulated polar sky images with and without SAI for each stratospheric aerosol type. High Sun and Twilight correspond to solar zenith angles of 29° and 96° respectively. No SAI corresponds to 0 W m^{-2} and the highest loading amount corresponds to −4 W m^{-2} of radiative forcing. For each aerosol, each column corresponds to the 10th, 50th, and 90th percentile population-weighted tropospheric AOD values.

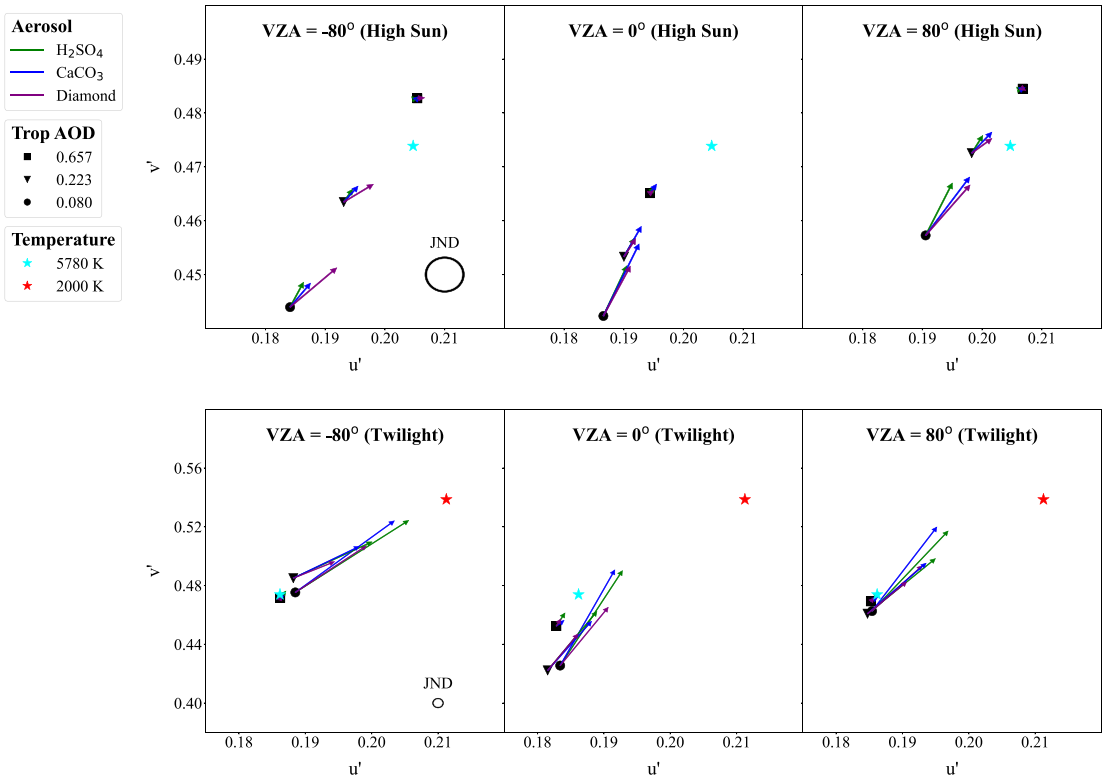

Figure 4. Chromaticity diagrams in the 1976 CIE *u'v'* plane. Chromaticity points corresponding to principal plane sky color are plotted for the 10th, 50th, and 90th percentile population-weighted tropospheric AOD values at three viewer zenith angles (VZA). Sky color without SAI corresponds to the black shapes. Arrows plotted for each aerosol type start from points without SAI and end at points with added −2 W m^{-2} of SAI for the same tropospheric AOD. During High Sun and Twilight, the sun is positioned at VZA = 29° and 96° respectively. The color of blackbody temperatures 5780 K and 2000 K represent white (blue star) and red (red star) respectively.

due to both its larger particle size and larger optical depth.

In figures 5 and 6, we also see respectively the chromaticity and brightness changes due to increasing tropospheric AOD from the 10th to 50th percentile population-weighted value without SAI (see more in figure D5). This leads to chromaticity and brightness changes with a similar spatial distribution but larger magnitudes than adding −2 W m^{-2} of SAI. This applies to all three aerosol types, apart from the region near the sun where H_2SO_4 and $CaCO_3$ each increases brightness three to five times more than

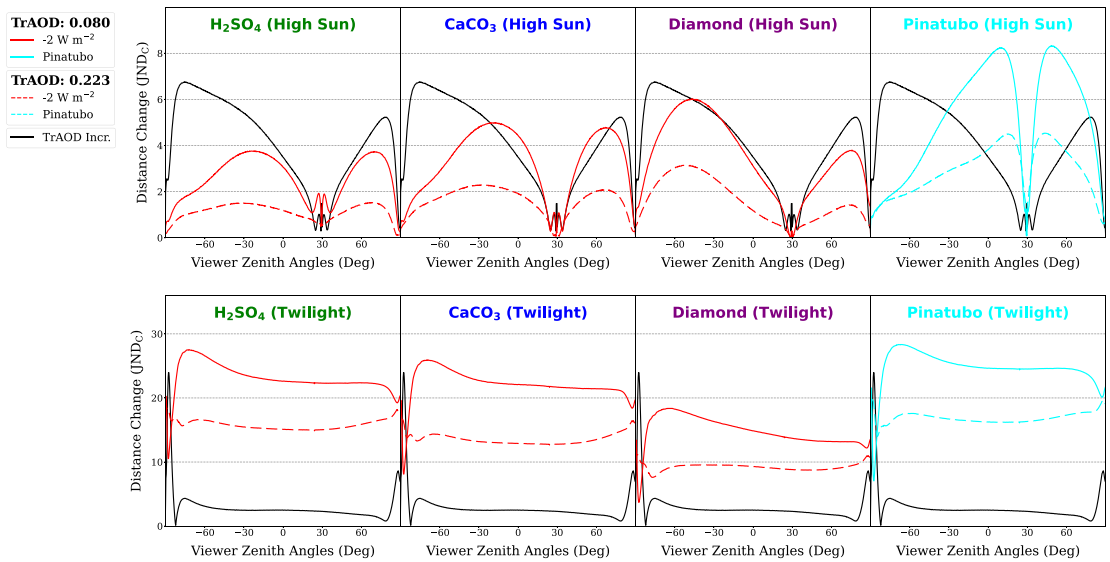

Figure 5. Principal plane sky color change from SAI in units of just noticeable difference in color (JND_C) versus viewer zenith angle for each aerosol type. Plotted are changes due to SAI at -2 W m^{-2} of radiative forcing and Pinatubo for comparison. During High Sun and Twilight, the sun is positioned at viewer zenith angle 29° and 96° respectively. Non-black solid and dashed lines correspond respectively to the 10th and 50th percentile tropospheric aerosol optical depth (TrAOD) conditions. The black lines show the color change due to increasing TrAOD from the 10th to 50th percentile values without SAI.

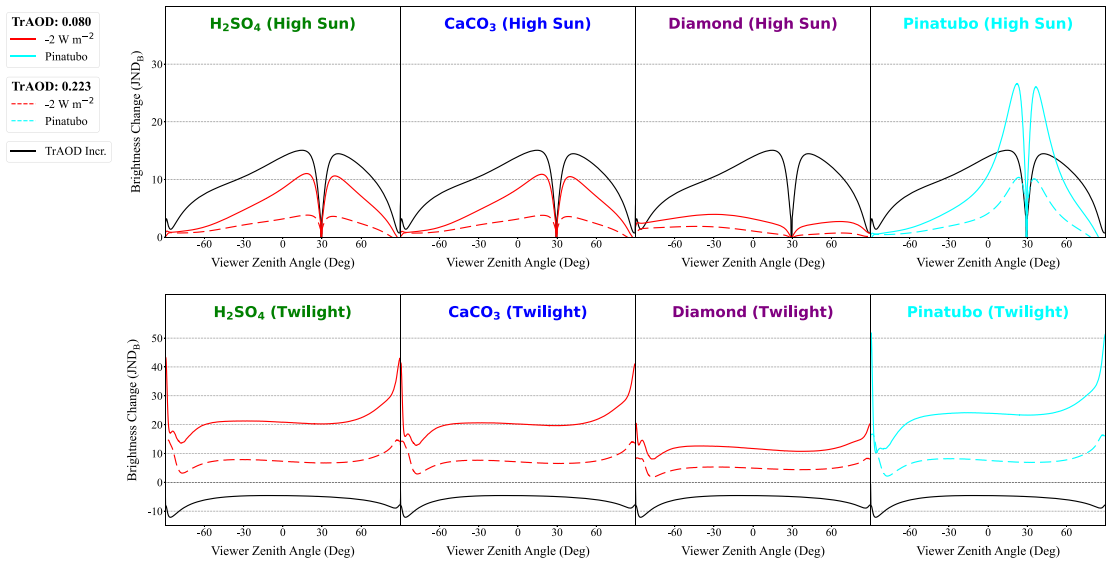

Figure 6. Principal plane sky brightness change from SAI in units of just noticeable difference in brightness (JND_B) versus viewer zenith angle for each aerosol type. Plotted are changes due to SAI at -2 W m^{-2} of radiative forcing and Pinatubo for comparison. During High Sun and Twilight, the sun is positioned at viewer zenith angle 29° and 96° respectively. Non-black solid and dashed lines represent respectively the 10th and 50th percentile tropospheric aerosol optical depth (TrAOD) conditions. The black lines show the brightness change due to increasing TrAOD from the 10th to 50th percentile values without SAI.

diamond. Therefore, adding SAI largely leads to high sun visual impacts akin to adding pollution, in agreement with Kravitz *et al* [9].

During twilight, visual impacts of tropospheric aerosol are sharply distinct from those of SAI since the sun is primarily illuminating the stratosphere while much of the troposphere is shaded. With the sun below the horizon, increasing tropospheric aerosol has mostly a dimming effect since the intensity of light traveling to the observer from the illuminated stratospheric aerosol is diminished by tropospheric scattering.

4. Discussion and conclusion

Understanding the visual impact of SAI on the sky's appearance could play an important role in shaping the public's attitude towards its deployment. We summarized SAI's impact on sky appearance in the previous section, linking it to measurements of a

JND, the smallest change in color or intensity perceptible by observers matching two side-by-side color or brightness levels in controlled experiments. We expect noticeability thresholds to be larger in the real world without side-by-side comparisons. In this section, we discuss the extent to which these changes may be noticed in practice.

First, consider the impacts of sulfate SAI at -2 W m^{-2} during daytime. Changes in sky color would be undetectable by roughly half of randomly chosen observers because the tropospheric aerosol is sufficient to keep color changes from SAI below 1 JND_C. For cleaner tropospheric conditions, we can compare the color gradient in a natural sky to color changes from SAI. For our high sun scenario with the sun at zenith angle 29°, the bluest part of the sky is about 60° above the horizon opposite the sun (see figure D4). The color difference between that point and the white point shown in figure 4 is approximately 16 JND_C. For the 10th percentile tropospheric AOD, the maximum color change is just under 4 JND_C, so SAI shifts blue tones about a quarter of the distance to white. Where the sky is naturally bluer, this would be perceived as turning darker blues to lighter blues more like those normally seen at lower elevation angles (see figure D6). Where the sky is naturally whiter, the color change due to SAI would be perceived as whitening.

Suppose -2 W m^{-2} of SAI were implemented over a quarter century, faster than is considered in many scenarios [36]. Human memory augmented by photographs would play an important role in determining what fraction of observers notices changes in the daytime sky. Our guess is that particularly astute observers might be able to notice sky color changes under particularly low levels of tropospheric aerosols if aided by photographs or printed color chips. However, given the relatively small color change in JND_C units, it seems unlikely that observers would notice color changes even under unpolluted skies. Yet at -4 W m^{-2} of SAI with comparatively large sulfate aerosol, sky whitening would be larger than that of Pinatubo consistent with Kravitz *et al* [9], and more than twice as noticeable as the -2 W m^{-2} whitening found here.

Brightness increases during high sun are greatest near the sun yet extend across the full extent of the sky at lesser amounts. The solar aureole generally lies within approximately a 30° radius of the sun. The inner aureole is too bright to gaze at without eye protection. However, the outer portion may more readily be seen underneath the sun, closer to the sun with peripheral vision, or when the sun itself is blocked by a physical obstruction. We expect brightening and enlargement of the solar aureole to be more noticeable than sky color changes because the peak brightness change is twice as large as the peak color change in JND units. Also, the aureole is a feature whose size can be judged more readily than a shift in blueness of the sky without a reference.

During twilight, we expect that changes would be noticeable to all except a small fraction of the population living in the most polluted atmospheric conditions. However, we are unable to evaluate what fraction of people would notice these changes. This depends heavily on human behavior, such as how often people can observe the sky at twilight despite light pollution and physical obstructions.

Our noticeability discussion applies roughly equally to calcite SAI, since the calcite aerosol exhibits sufficiently similar scattering properties to that of the sulfate aerosol. Diamond SAI is substantially different, however. During the day, it exhibits slightly stronger color changes and substantially less sky brightening. During twilight, it causes substantially less sky reddening.

Our conclusions are subject to several caveats. First, the original MacAdam ellipses on which our JND_C metric is based were determined by recording measurements from only a single observer [10, 37]. We expect some degree of imprecision in our JND_C arising from both the original ellipses and the further approximated *u'v'* circles.

We only simulate cloudless skies. The addition of cloud cover in its various forms could either reduce or enhance the visibility of SAI. For instance, since we expect SAI to cause some level of whitening, white clouds typical of a sunny day could provide less contrast than in a perfectly clear sky. Hence, they might lessen the noticeability of SAI. On the contrary, dark storm clouds could provide increased contrast and hence increase noticeability. If SAI noticeably reddens the sky during sunset and twilight, clouds with their high reflectance might enhance the visuals of this effect. Clouds could provide a more absolute reference frame to evaluate sky color.

We only consider how the sky might look from the vantage point of a ground observer near sea level. We do not analyze if a reduction in shadows due to increased diffuse light might be noticeable in our ground level surroundings. We also do not consider how the sky might look from high altitude viewpoints such as mountains, tall buildings, or even airplanes. From these viewpoints, one might expect increased visibility of SAI due to lower AODs and less Rayleigh scattering between the viewer and the added stratospheric aerosol layer.

We do not investigate night sky degradation from scattered starlight and artificial lights by SAI. Nor do we consider how visibility of SAI would increase as pollution is reduced. Note however that the 10th percentile tropospheric AOD represents more typical conditions in a number of countries with relatively low air pollution, given the characteristics of the global population weighting we used.

We also do not investigate noticeability at fixed locations nor the effect of people traveling between

various locations. Tropospheric conditions are variable, and the range of experienced daily AODs is larger for more polluted regions (see figure B2 and table B1). Therefore, the likelihood of noticing visual impacts of SAI will be higher for some days of the year, even in polluted areas. However, urban AOD variation is larger than SAI AODs as noted by Kravitz *et al* [9], so attributing changes to SAI may be difficult.

Finally, and most fundamentally, radiative transfer calculations alone cannot determine how often or in what situations people might visually notice SAI deployment. Experimental tests with actual observers, possibly in a virtual reality space or planetarium, could provide a better understanding of how perceptible sky appearance changes due to SAI might truly be to the everyday, casual observer. Virtual reality would allow for three-dimensional representations of the sky and landscape, providing more realistic experiences than the two-dimensional counterparts presented here. Randomized images, rather than side-by-side comparisons, can better gauge the noticeability of changes [11]. Additional psychophysical experimental techniques might be employed to understand the effect of human memory on noticeability thresholds for sky visuals [38] along with the effects of SAI induced sky changes on subjective well-being [39, 40].

Data availability statement

The data that support the findings of this study are openly available at the following URL/DOI: https://doi.org/10.7910/DVN/RZ5P4I.

Acknowledgment

Ansar Lemon received support from Harvard's Solar Geoengineering Research Program. We would like to heavily thank Peter Irvine for connecting us with Steve Albers. We extend much gratitude to Benjamin Kravitz, Peter Irvine, and John Dykema for helpful feedback on our early draft. We thank John Dykema for helpful feedback on radiative forcing calculations. We also thank Joan Aguilar Fargas for his assistance with creating the web application for viewing the simulation results.

ORCID iDs

Ansar Lemon https://orcid.org/0009-0009-2306-3032
David W Keith https://orcid.org/0000-0002-8224-3780
Steve Albers https://orcid.org/0000-0002-7626-1384

References

[1] Tilmes S *et al* 2020 Reaching 1.5 and 2.0 °C global surface temperature targets using stratospheric aerosol geoengineering *Earth Syst. Dyn.* **11** 579–601
[2] Ji D, Fang S, Curry C L, Kashimura H, Watanabe S, Cole J N, Lenton A, Muri H, Kravitz B and Moore J C 2018 Extreme temperature and precipitation response to solar dimming and stratospheric aerosol geoengineering *Atmos. Chem. Phys.* **18** 10133–56
[3] Moore J C, Greve R, Yue C, Zwinger T, Gillet-Chaulet F and Zhao L 2023 Reduced ice loss from Greenland under stratospheric aerosol injection *J. Geophys. Res.-Earth Surf.* **128** e2023JF007112
[4] Richter J H, Tilmes S, Mills M J, Tribbia J J, Kravitz B, MacMartin D G, Vitt F and Lamarque J F 2017 Stratospheric dynamical response and ozone feedbacks in the presence of SO_2 injections *J. Geophys. Res.-Atmos.* **122** 12,557–73
[5] Eastham S D, Weisenstein D K, Keith D W and Barrett S R H 2018 Quantifying the impact of sulfate geoengineering on mortality from air quality and UV-B exposure *Atmos. Environ.* **187** 424–34
[6] Kravitz B *et al* 2014 A multi-model assessment of regional climate disparities caused by solar geoengineering *Environ. Res. Lett.* **9** 074013
[7] Robock A 2008 20 reasons why geoengineering may be a bad idea *Bull. At. Sci.* **64** 14–18
[8] Kolbert E 2022 *Under a White Sky: The Nature of the Future* Paperback edn (Crown) p 242
[9] Kravitz B, MacMartin D G and Caldeira K 2012 Geoengineering: whiter skies? *Geophys. Res. Lett.* **39** L11801
[10] CIE (Commission Internationale de l'Eclairage) 2014 Technical note 001:2014 *Chromaticity Difference Specification for Light Sources* (available at: https://cie.co.at/publications/chromaticity-difference-specification-light-sources)
[11] Hu W and Davis W 2016 Dimming curve based on the detectability and acceptability of illuminance differences *Opt. Express* **24** A885–97
[12] Albers S, Saleeby S M, Kreidenweis S, Bian Q, Xian P, Toth Z, Ahmadov R, James E and Miller S D 2020 A fast visible-wavelength 3D radiative transfer model for numerical weather prediction visualization and forward modeling *Atmos. Meas. Tech.* **13** 3235–61
[13] Raymond L, Lee J, Meyer W and Hoeppe G 2011 Atmospheric ozone and colors of the Antarctic twilight sky *Appl. Opt.* **50** F162–71
[14] Lange A, Rozanov A and von Savigny C 2023 Revisiting the question "why is the sky blue?" *Atmos. Chem. Phys.* **23** 14829–39
[15] Pope F D, Braesicke P, Grainger R G, Kalberer M, Watson I M, Davidson P J and Cox R A 2012 Stratospheric aerosol particles and solar-radiation management *Nat. Clim. Change* **2** 713–9
[16] Weisenstein D K, Keith D W and Dykema J A 2015 Solar geoengineering using solid aerosol in the stratosphere *Atmos. Chem. Phys.* **15** 11835–59
[17] Dykema J A, Keith D W and Keutsch F N 2016 Improved aerosol radiative properties as a foundation for solar geoengineering risk assessment *Geophys. Res. Lett.* **43** 7758–66
[18] Weisenstein D K, Visioni D, Franke H, Niemeier U, Vattioni S, Chiodo G, Peter T and Keith D W 2022 An interactive stratospheric aerosol model intercomparison of solar geoengineering by stratospheric injection of SO_2 or accumulation-mode sulfuric acid aerosols *Atmos. Chem. Phys.* **22** 2955–73
[19] Guasta M D, Morandi M, Stefanutti L, Stein B and Wolf J P 1994 Derivation of Mount Pinatubo stratospheric aerosol mean size distribution by means of a multiwavelength lidar *Appl. Opt.* **33** 5690–7

[20] Russell P B *et al* 1996 Global to microscale evolution of the Pinatubo volcanic aerosol derived from diverse measurements and analyses *J. Geophys. Res.-Atmos.* **101** 18745–63
[21] Clough S A, Shephard M W, Mlawer E J, Delamere J S, Iacono M J, Cady-Pereira K, Boukabara S and Brown P D 2005 Atmospheric radiative transfer modeling: a summary of the AER codes *J. Quant. Spectrosc. Radiat. Transfer* **91** 233–44
[22] Iacono M J, Delamere J S, Mlawer E J, Shephard M W, Clough S A and Collins W D 2008 Radiative forcing by long-lived greenhouse gases: calculations with the AER radiative transfer models *J. Geophys. Res.-Atmos.* **113** D13103
[23] Intergovernmental Panel On Climate Change (Ipcc) 2023 *Climate Change 2021—The Physical Science Basis: Working Group I Contribution to the Sixth Assessment Report of the Intergovernmental Panel on Climate Change* 1st edn (Cambridge University Press) (available at: www.cambridge.org/core/product/identifier/9781009157896/type/book) (Accessed August 2024)
[24] Govindasamy B and Caldeira K 2000 Geoengineering Earth's radiation balance to mitigate CO_2-induced climate change *Geophys. Res. Lett.* **27** 2141–4
[25] Keith D W and MacMartin D G 2015 A temporary, moderate and responsive scenario for solar geoengineering *Nat. Clim. Change* **5** 201–6
[26] Spafford L and MacDougall A H 2020 Quantifying the probability distribution function of the transient climate response to cumulative CO_2 emissions *Environ. Res. Lett.* **15** 034044
[27] Kato S, Rose F G, Rutan D A, Thorsen T J, Loeb N G, Doelling D R, Huang X, Smith W L, Su W and Ham S-H 2018 Surface irradiances of edition 4.0 clouds and the Earth's radiant energy system (CERES) energy balanced and filled (EBAF) data product *J. Clim.* **31** 4501–27
[28] Loeb N G, Doelling D R, Wang H, Su W, Nguyen C, Corbett J G, Liang L, Mitrescu C, Rose F G and Kato S 2018 Clouds and the Earth's radiant energy system (CERES) energy balanced and filled (EBAF) top-of-atmosphere (TOA) edition-4.0 data product *J. Clim.* **31** 895–918
[29] Jones A C, Hawcroft M K, Haywood J M, Jones A, Guo X and Moore J C 2018 Regional climate impacts of stabilizing global warming at 1.5 K using solar geoengineering *Earth's Future* **6** 230–51
[30] Kleinschmitt C, Boucher O and Platt U 2018 Sensitivity of the radiative forcing by stratospheric sulfur geoengineering to the amount and strategy of the SO_2 injection studied with the LMDZ-S3A model *Atmos. Chem. Phys.* **18** 2769–86
[31] Pawson S and (Global Modeling And Assimilation Office) 2015MERRA-2 inst3_2d_gas_Nx: 2d,3-hourly, instantaneous, single-level, assimilation, aerosol optical depth analysis V5.12.4. *NASA Goddard Earth Sciences Data and Information Services Center* (available at: https://disc.gsfc.nasa.gov/datacollection/M2I3NXGAS_5.12.4.html) (Accessed 16 Febuary 2024)
[32] Center For International Earth Science Information Network-CIESIN-Columbia University 2018 Gridded population of the world, version 4 (GPWv4): population density adjusted to match 2015 revision UN WPP Country totals, revision 11 (available at: https://sedac.ciesin.columbia.edu/data/set/gpw-v4-population-density-adjusted-to-2015-unwpp-country-totals-rev11) (Accessed 27 March 2024)
[33] Solomon S, Daniel J S, Neely R R, Vernier J-P, Dutton E G and Thomason L W 2011 The persistently variable "background" stratospheric aerosol layer and global climate change *Science* **333** 866–70
[34] Gelaro R *et al* 2017 The modern-era retrospective analysis for research and applications, version 2 (MERRA-2) *J. Clim.* **30** 5419–54
[35] Vos J J 1978 Colorimetric and photometric properties of a 2° fundamental observer *Color Res. Appl.* **3** 125–8
[36] Richter J H, Visioni D, MacMartin D G, Bailey D A, Rosenbloom N, Dobbins B and Lamarque J F 2022 Assessing responses and impacts of solar climate intervention on the Earth system with stratospheric aerosol injection (ARISE-SAI): protocol and initial results from the first simulations *Geosci. Model Dev.* **15** 8221–43
[37] MacAdam D L 1942 Visual sensitivities to color differences in daylight* *J. Opt. Soc. Am.* **32** 247–74
[38] Lee B and Harris J 1996 Contrast transfer characteristics of visual short-term memory *Vis. Res.* **36** 2159–66
[39] Li Y, Guan D, Tao S, Wang X and He K 2018 A review of air pollution impact on subjective well-being: survey versus visual psychophysics *J. Clean. Prod.* **184** 959–68
[40] Li Y, Guan D, Yu Y, Westland S, Wang D, Meng J, Wang X, He K and Tao S A psychophysical measurement on subjective well-being and air pollution 2019 *Nat. Commun.* **10** 5473